TIME-SERIES ENSEMBLE PHOTOMETRY OF THE HIGH-AMPLITUDE δ SCUTI STAR AE URSAE MAJORIS

by

Joel Winner Jolley

A senior thesis submitted to the faculty of

Brigham Young University

in partial fulfillment of the requirements for the degree of

Bachelor of Science

Department of Physics and Astronomy

Brigham Young University

August 2007

BRIGHAM YOUNG UNIVERSITY

DEPARTMENT APPROVAL

of a senior thesis submitted by

Joel Winner Jolley

This thesis has been reviewed by the research advisor, research coordinator, and department chair and has been found to be satisfactory.

Date	Michael Joner, Advisor
Date	Eric Hintz, Research Coordinator
Date	Ross Spencer, Department Chair

ABSTRACT

TIME-SERIES ENSEMBLE PHOTOMETRY OF THE HIGH-AMPLITUDE δ SCUTI STAR AE URSAE MAJORIS

Joel Winner Jolley

Department of Physics and Astronomy

Senior Thesis

This research presents time-series photometric data on the short-period, double-mode δ Scuti star AE Ursae Majoris based on new observations from 2007. Archival data from 1974 onward are used to evaluate reported period changes. There are 19 new times of maximum light with six times observed simultaneously on more than one telescope. Forty-three times of maximum light published from 2002 through 2006 have been incorporated into this research making a total of 62 new times of maximum used for period determinations. The ephemeris from Broglia & Conconi (1975) was corrected giving a new ephemeris of $\mathrm{HJD}_{max} = 2442062.58205 + 0.0860170734 \times E$ from which O-C values are reported. The observations and analysis support the previous findings of Pócs & Szeidl (2001) and Zhou (2001) that the period of AE UMa has been constant over the past 33 years with a corrected value of $P_0 = 0^d.0860170734$. This data refutes the quickly decreasing period found by Hintz et al. (1997) of $-1.14 \times 10^{-10} dd^{-1}$. Through Fourier analysis we calculated the first overtone period $P_1 = 0^d.066528768$ and determined frequencies $f_0 = 11.6256845$ and $f_1 = 15.0310915$ corresponding to the two periods.

ACKNOWLEDGMENTS

Acknowledgments are so well deserved by so many people who have made this thesis a reality. Nothing would have been done without the help of my mentor and long-time friend, Professor Michael Joner. I thank him for accepting my help with his research and holding my hand through the whole project.

Thanks are also in order for other faculty in the department of astronomy who have taught me the principles behind this research and assisted in the data analysis: Dr. Eric Hintz, Dr. Benjamin Taylor, and Dr. Clark Christensen. Some of the data used to write this thesis were obtained and manipulated by other students in the astronomy department, namely Summerdale, Laura, Craig and Whitney. Special help was received by Jacob Albretson, a graduate student in the department, and Lisa Joner, wife to Professor Joner.

I would like to thank my family. My parents Greg and Marilee Jolley gave me the basis for everything I have done. They taught me more than anyone ever has. And finally, thanks to my wonderful wife Kari, who has supported me and sacrificed more than I have to help me complete this project. She is the motivation for everything I do and I love her.

Contents

List of Tables

List of Figures

Chapter 1

Introduction and Background

1.1 About AE Ursae Majoris

The variable star AE Ursae Majoris is located under Epoch 2000 coordinates at right ascension $\alpha_{2000} = 09^h36^m53^s$ and declination $\delta_{2000} = +44°04'01''$. The star has visual magnitude in the range $m_V = 10.86-11.52$ and A9 spectral type with a primary pulsation period $P_0 = 0^d.0860$. The star has been studied several times since Geyer et al. (1955) reported on its variability. Tsesevich (1956), Tsesevich (1973), and Filatov (1960) observed the star visually, reporting ten times of maximum light. Tsesevich (1973) determined that the star was a dwarf Cepheid with significant amplitude variation on a short time scale. Since the time the variability was determined, the star has been studied by Szeidl (1974), Broglia & Conconi (1975), Braune et al. (1979) and Rodríguez et al. (1992). The Bundesdeutsche Arbeitsgemeinschaft für Veränderliche Sterne (BAV) group from Germany has observed this star many times since 1979, publishing many times of maximum light (Braune et al. (1979), Braune & Mundry (1982), **?**, Hübscher et al. (1992), Hübscher et al. (2005), Agerer et al. (1999), Agerer & Hübscher (2003), Hübscher (2005), and Hübscher & Walter (2007)). Finally, in 2006, 8 times of maximum light were published by Bíró et al. (2006), Klingenberg et al. (2006), and Hübscher et al. (2006). Appendix A lists all observed times of maximum light for AE UMa from 1937 to the present, including all the maxima from 2002 onward as well as our new data obtained in 2007.

Hintz et al. (1997) used time-series ensemble photometry to obtain six new times of maximum light and together with archival data concluded that the period of AE Uma was decreasing at the rate of $-1.14 \times 10^{-10} dd^{-1}$. If correct, the rapid period decrease would be the fastest known period change of a dwarf Cepheid. Contrary to Hintz et al. (1997), Pócs & Szeidl (2001) reported that the fundamental period

of AE UMa had not changed significantly over the past 60 years with a value of $P_0 = 0^d.086017059 \pm 1 \times 10^{-9}$. Later that year Zhou (2001) backed the results of Pócs & Szeidl (2001) with new data and a new period determination of $P_0 = 0^d.086017066$. Both papers refuted the results of Hintz et al. (1997) but only Zhou (2001) attempted to explain why Hintz et al. (1997) might be wrong. Zhou (2001) concluded that it was because the 1997 data set was very limited, spanning only three nights and 10 times of maximum light.

AE UMa is a double mode variable star. This means that at least two frequencies contribute to the star's periodicity and amplitude. The most recent period determination was reported in Zhou (2001). It was reported that the fundamental or primary period ($P_0 = 0^d.08617066$) remained essentially constant since Broglia & Conconi (1975) reported $P_0 = 0^d.086016883$. Zhou (2001) obtained a first overtone period of $P_1 = 0^d.066527$. Both Zhou (2001) and Pócs & Szeidl (2001) reported that the first overtone period was decreasing at the rates of $1.8 \pm 9.1 \times 10^{-9} y^{-1}$ and $-0.13 \pm 0.14 \times 10^{-6} y^{-1}$, respectively.

1.2 Motivation

The information contained in the preceding section constitutes the most significant research performed on AE UMa as of the time of this publication. These investigations into the beat phenomenon of AE UMa have revealed the two periods, P_0 and P_1, and their associated frequencies at $f_0 = 11.625600 cd^{-1}$ and $f_1 = 15.03149 cd^{-1}$. No research has been performed to find higher order periods and frequencies, but the possibility still exists and is suggested by Pócs & Szeidl (2001). In our research we will attempt to confirm these periods and detect any period changes. The particular cause of the radial variability of AE UMa has been attributed to evolutionary effects of the post main sequence stars, though there is currently no definitive answer to this question.

This research will help in understanding how stars function and evolve over their life cycles. It is important to study many different stellar effects. This can help

determine where stars are in their life cycle and what is causing them to behave in various ways. It is possible that other stars maintain solar systems in which planets form and can potentially sustain life. Our own sun is a star in the middle of the Population I main sequence. AE UMa's radius is expanding and contracting, causing the visual magnitude to change in a periodic manner. Knowing more about this pulsation and how it occurs will help us to understand what is happening in other stars, including our own sun.

This project is intended to continue the research on AE UMa and to assist in better understanding the nature of stellar variability. There are other stars in the universe that share their properties with AE UMa. Understanding what these stars are doing will contribute to our understanding of how the universe works and evolves.

1.3 Star field of AE UMa

AE UMa is a variable star located in the constellation Ursae Majoris. This constellation is commonly known as the Big Bear and contains the asterism known as the Big Dipper. AE UMa is the 86^{th} variable star found in Ursae Majoris. The naming convention for variable stars is very complicated. For AE UMa, "AE" is the star designator and "Ursae Majoris" is the constellation in which the star is found. In general the first variable star in a constellation is designated "R." Those that follow are labeled "S", "T" and so on up to "Z." Each star after "Z" is named "RR" to "RZ", followed by "SS" to "SZ" all the way to "ZZ." After that, stars are labeled "AA" to "AZ", then "BB" to "BZ" all the way to "QZ." The letter "J" is not used in order to avoid any confusion with "I." There are 334 letter combinations, so any variable stars after the 334^{th} are labeled "V 335", then "V 336" and so on.

Surrounding AE UMa there are five stars in each image that we selected to use as reference stars for comparison purposes. These stars constitute a comparison ensemble. They should have no detected variability so they are used as zero points for magnitude comparisons in order to obtain differential magnitudes. This will be discussed later in the data analysis section. During the data analysis, only three

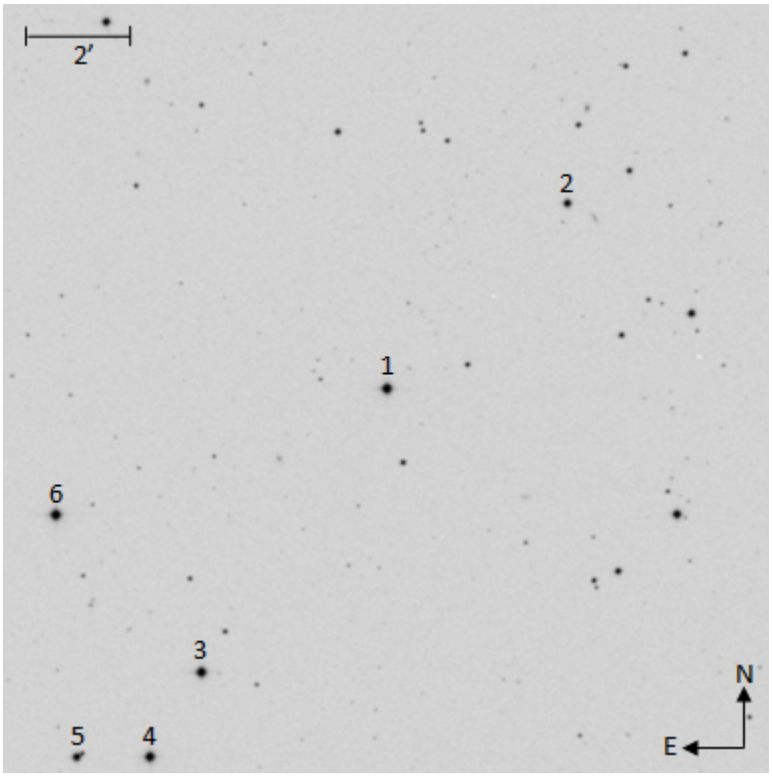

Figure 1.1: The star field seen on the Tenagra telescope centered on star 1, which is AE UMa.

comparison stars were retained in the comparison ensemble because two of them contained errors too large for valid comparisons.

Between May and June 2007 five comparison stars and AE UMa were observed for several hours each night, obtaining thousands of object frames. Most images were taken in the visual (V), or green, filter with a few taken in blue (B) and red (R) filters. Most of the work done in this research used only the V filter images. Figures 1.1 and 1.2 below designate AE UMa and the comparison stars that were observed. Figure 1.1 is an image similar to those from the Orson Pratt Observatory and Tenagra Observatory, while Figure 1.2 is an image similar to those from the West Mountain Observatory.

There are two main differences between Figures 1.1 and 1.2. First, the numbers associated with each star are in a different order. This is due to the order of star

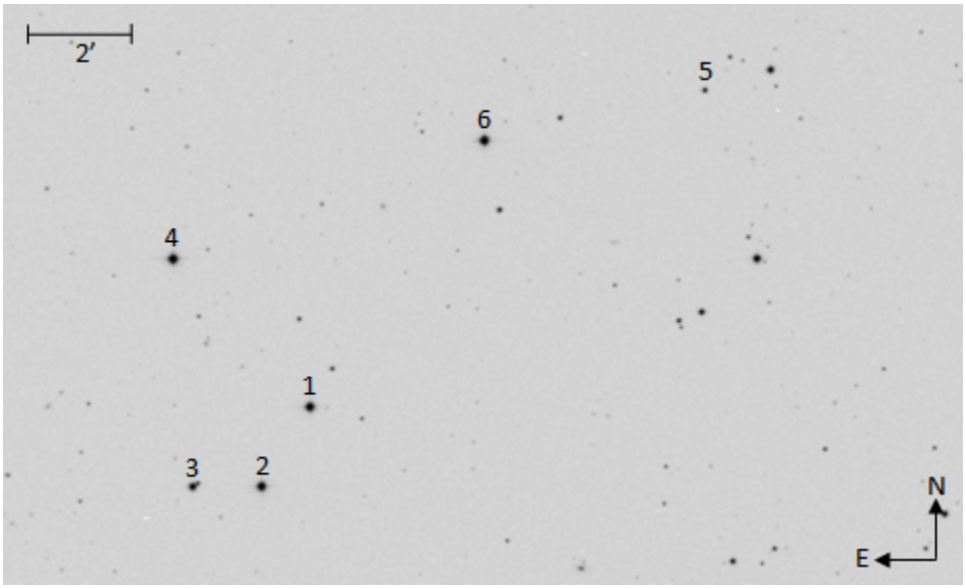

Figure 1.2: The star field seen on the West Mountain Observatory telescopes centered on star 6, which is AE UMa.

selection when the data was being analyzed. The reason for this is that some of the data was previously analyzed with aperture photometry (See Sec. 3.4). This is merely a procedural difference and has no bearing on the results. The second difference is that the star labeled "2" in Figure 1.1 is not visible in Figure 1.2. This is because the different telescope cameras have different fields of view (See Table 2.2). Therefore, a different star was used in Figure 1.2 and is labeled "5" in that figure. This also has no difference on the outcome of the results because both star 2 from Figure 1.1 and star 5 from Figure 1.2 were not used in the comparison ensemble when determining the differential magnitudes. This will be explained later in the data analysis section (see Sec. 3.5).

Chapter 2

Equipment and Observations

2.1 Tenagra Observatory

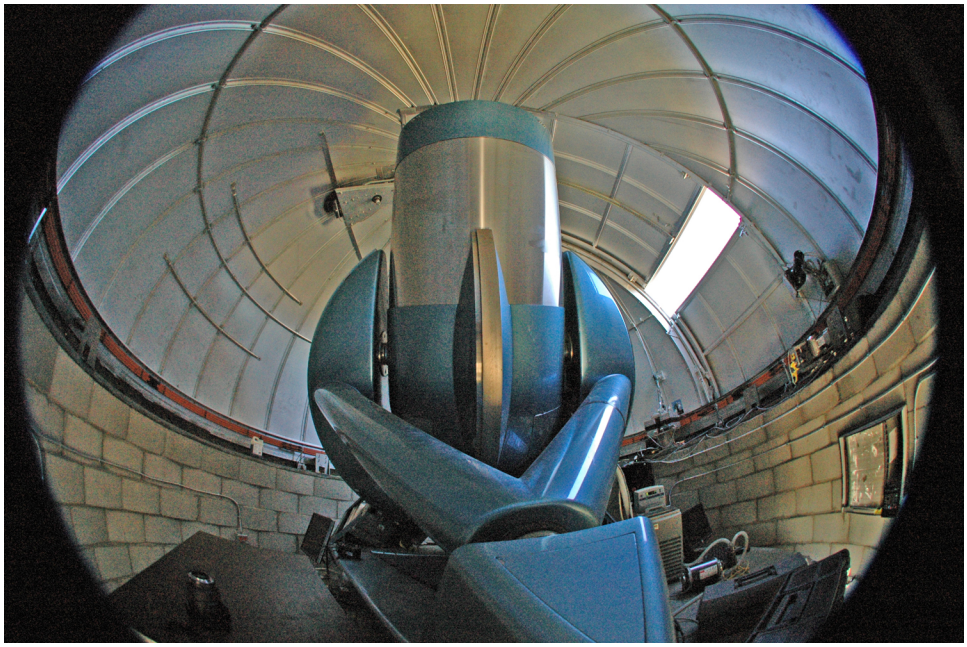

Figure 2.1: The Tenagra II 32-in telescope at the southern Arizona site of Tenagra Observatories. Tenagra Observatories (2007)

Tenagra Observatories, Ltd. is a group of privately owned telescopes located in southern Arizona, Oregon, Norway and western Australia. The telescope used for this research was the Tenagra II, which is located in southern Arizona. This telescope is a 0.81 meter (32-in) f/7 Ritchey-Chretien. Because the telescope is completely automated, astronomers from remote locations are able to submit observation requests. The telescope takes the images and saves them to a secure database. The astronomer requesting the observation has a login and is able to then access the images that he

specifically ordered. Eleven nights of data were secured on the Tenagra II telescope obtaining seven maxima, two of which were recorded on the WMO telescopes. Table 2.1 lists the times of maximum recorded on more than one telesope, and Fig. 2.2 is a graph of the three sets of data for HJD 2454230.

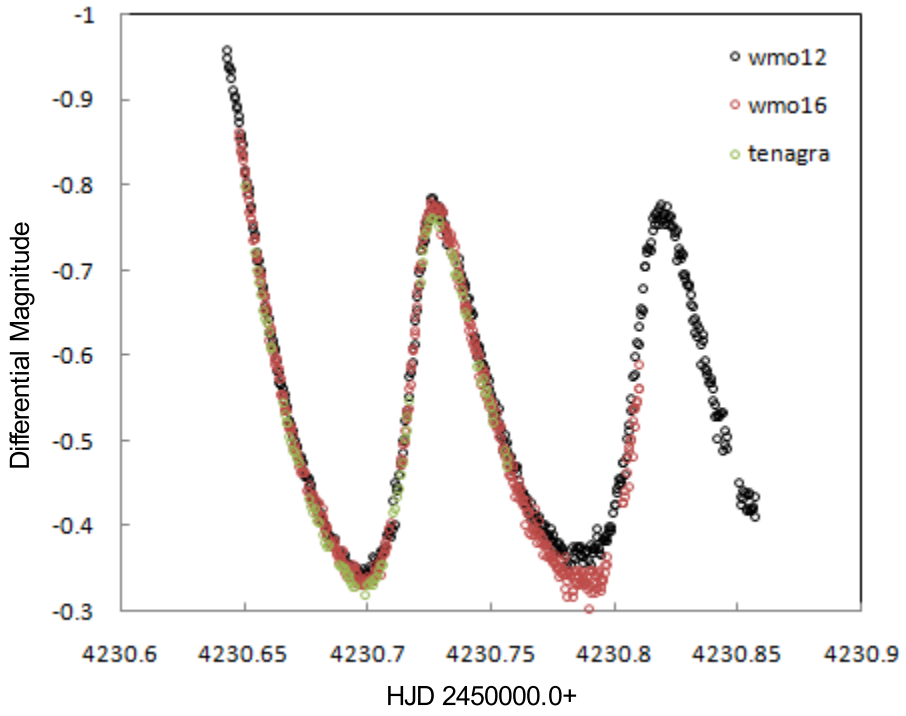

Figure 2.2: The light curve of AE UMa that was recorded on three different telescopes.

The site at Tenagra is located at longitude west $110°52'44.8''$ and latitude $+31°27'44.4''$ at an altitude of 4,306 feet. It has excellent seeing, with typical nights reaching 2 in Full Width at Half Maximum (FWHM). (See Sec. 3.4 for an explanation of FWHM.) The telescope is equipped with a SITe S103xA Charge-Coupled Device (CCD), more commonly called a detector. The telescope and CCD specifications for this and other telescopes used in this research are given in Table 2.2.

Table 2.1. Times of Maximum Observed on Multiple Telescopes

$HJD_{max}2400000.0+$	Tenagra II	WMO 16 inch	WMO 12 inch
54229.70		X	X
54230.73	X	X	X
54235.72	X	X	X
54236.67		X	X
54236.75		X	X
54246.73		X	X

Table 2.2. Specifications for Telescope and CCD Combinations

	Tenagra II S103xA	WMO 16 in STL-1301E	WMO 12 in ST-10XME	OPO ST-10XME
Diameter	$810mm$ $(32in)$	$406mm$ $(16in)$	$203mm$ $(12in)$	$406mm$ $(16in)$
Focal Ratio	f/7	f/10	f/9	f/4
Focal Length	$5690m$ $(224in)$	$4060mm$ $(160in)$	$1827mm$ $(108in)$	$1626mm$ $(64in)$
Plate Scale	$36.25^{''}mm^{-1}$	$50.8^{''}mm^{-1}$	$75.2^{''}mm^{-1}$	$126.5^{''}mm^{-1}$
Pixel Size	24 μm	16 μm*	6.8 μm*	6.8 μm
CCD Size	24.6 x 24.6 mm^2	20.5 x 16.4 mm^2	14.7 x 10 mm^2	14.7 x 10 mm^2
Imaging Array	1024 x 1024 pixels	1280 x 1024 pixels*	2184 x 1472 pixels*	2184 x 1472 pixels
Field of View	$14.85^{'}$ x $14.85^{'}$	$17.3^{'}$ x $13.9^{'}$	$18.4^{'}$ x $12.5^{'}$	$31.3^{'}$ x $21.1^{'}$
Resolution/Pixel	$0.87^{''}$	$0.81^{''}$*	$0.51^{''}$*	$0.86^{''}$

* The CCDs on the WMO telescopes were binned 2X2 in order to make larger pixels for faster download times. This creates an effective pixel size of $32\mu m$ for the STL-1301E and $13.6\mu m$ for the ST-10XME. This changes the imaging arrays to 640 x 512 and 1092 x 736, respectively, with the resolution per pixel changing to $1.62^{''}$ for the STL-1301E and $1.02^{''}$ for the ST-10XME.

2.2 West Mountain Observatory

Figure 2.3: West Mountain Observatory with three domes located at the top of West Mountain. Brigham Young University (2007)

West Mountain Observatory (WMO) seen in Figure 2.3 is located on the top of West Mountain located on the south end of Utah Lake, about one hour from Brigham Young University (BYU) at an elevation of 6,850 feet. The site enjoys good seeing, with typically 60 nights for all-sky photometry and 100 nights for differential photometry per year similar to the research reported in this paper. (See Sec. 2.5 for an explanation of all-sky photometry also known as photometric conditions.)

The observatory was built in 1981. A house for the resident astronomer was added in 1982 and is now used to house visiting observers. Two of the three telescopes at the observatory were used to collect data for this research: a carbon truss 12-in RC Optical Systems (RCOS) f/9 Ritchey-Chretien and the older 16-in Meade optical tube. The one telescope not used in this research is the 20-in f/8.1 RCOS Ritchey-Chretien optical tube. All three of these optical tubes are mounted on Paramount ME robotic mounts controlled by computer. Twelve nights of data were taken at the West

Mountain Observatory, five on the 12-in and seven on the 16 inch. We obtained 16 maxima with some duplicated on both the West Mountain 16-in and 12-in telescopes, as well as on the Tenagra telescope. The telescope and CCD specifications for the two West Mountain telescopes are given in Table 2.2 above.

2.3 Orson Pratt Observatory

Figure 2.4: The dome on top of the ESC that houses the David Derrick Telescope. Brigham Young University (2007)

The Orson Pratt Observatory (OPO) is located on the 5^{th} and 6^{th} floors of the Eyring Science Center (ESC) at BYU in Provo, Utah. The dome shown in Fig. 2.4 houses the 16-in David Derrick Telescope (DDT). The observatory is in the heart of Provo at an elevation of 4,720 feet. The DDT was installed on March 26, 1998. The telescope is used by faculty and students at the university and is a primary tool for the observational astronomy courses taught by the physics and astronomy department.

Two nights of data were recorded on the DDT, obtaining two new times of maximum light. The telescope and CCD specifications are given in Table 2.2.

2.4 Filters

Filters are used to examine a particular section of a star's spectrum. The most commonly used segment of spectrum is the visual segment. This includes all the colors that humans can see. For this research visual, red, and blue filters were used. These filters allow light in those regions to penetrate to the CCD while blocking all other light.

Stars radiate along the electromagnetic spectrum according to a curve established by Max Planck. This curve describes the radiation of a blackbody. A blackbody is a theoretical body that absorbs all radiation incident upon it while radiating energy back out according to the Planck curve. This curve shows the relative intensity of radiation according to wavelength on the electromagnetic spectrum. Though a blackbody is only theoretical, stars radiate at intensities nearly identical with a blackbody curve. A CCD uses a filter to isolate a small wavelength range and measure the star's intensity in that range. In our case this gives the star's visual, blue, or red magnitude.

When two different filters are used, for example the visual and blue filter, they each produce a different measurement of the star's brightness or magnitude. When these magnitudes are compared and one is subtracted from the other, a color index is obtained. This color index, for example blue-visual (B-V), can be used to obtain information about the star, especially the star's temperature. The color index is essentially a measure of the slope of the blackbody curve. This can be compared to the curves of various blackbodies at different temperatures (See Fig. 2.5) to determine which temperature curve fits the star's color index. This will give a very accurate temperature for the star.

Two of the most common filter sequences used in astronomy are the Johnson UBVRI system discussed in Bessell (1979) and the Strömgren *uvby* system discussed Crawford & Barnes (1970). The Johnson system is a broadband system with each

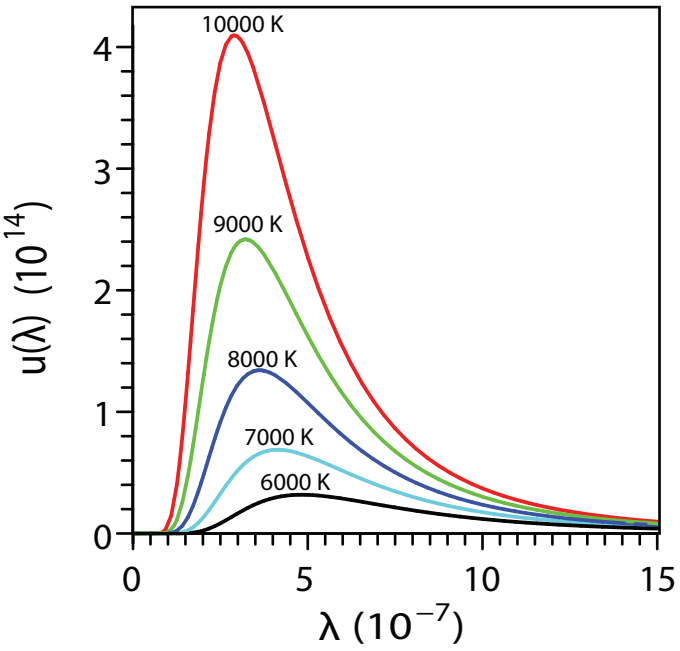

Figure 2.5: Blackbody curves at various temperatures relating intensity and wavelength. The visible part of the spectrum lies between 400 and 700 nm.

filter covering about 100 nm. This allows a lot of light to contact the CCD, making short exposure times. However, this system uses a broad spectral range which makes detailed spectral analysis difficult. The Strömgren system filters have only 20-30 nm bandpasses and require longer exposure times but allow the observer to study specific spectral features. Our study uses the Cousins version of the Johnson UBVRI system found in Cousins (1974). The observations have been done primarily in the V filter.

2.5 Imaging Devices

One of the basic parameters astronomers use is the magnitude of a star. Magnitude is a measure of how bright the star is at a specific wavelength. The way to determine this is to look at the star with some imaging device and measure how much light is received. Early astronomers used the eye. Hipparchus was the first to create a magnitude scale. He did this by observing the relative brightness of stars

with his eye. He gave the brightest stars a magnitude of 1 and the faintest stars a magnitude of 6. Looking at his scale, later astronomers determined that a difference of five magnitudes corresponded to 100 times difference in brightness. This showed that the human eye followed a logarithmic scale in responding to light. The easiest way to determine the magnitude of a star is to count the number of photons that are detected over a period of time.

The first devices to produce a recorded image were the photographic plates. These were able to record an image for later use and they have a linear response to incident light, which makes calculations easier. The problem with these plates is that they are only linear in a short wavelength range and possess a small dynamic range. Also, they are not very efficient at counting the number of incident photons. This efficiency is called quantum efficiency (QE) and is an important property of all imaging devices. The photographic plate has a quantum efficiency of only about 1%. This is very low and therefore requires long exposure times to obtain sufficient signal to noise ratios.

Eventually the photomultiplier (PM) came on the scene (See Fig 2.6). As its name indicates, the PM enhances the signal received from the star. It amplifies the incident photon count. This allows for shorter exposure times and greater QE. There are two major disadvantages to the PM. The first is that the PM can observe only one object at a time and not a field of stars. The second problem is that photometric conditions are required. A night will have photometric conditions only if every part of the sky is the same as every other part of the sky. This means that (1) the temperature needs to be uniform around the telescope, especially in and around the dome; (2) the light needs to be uniform in the sky, which might not be possible because of the moon or light pollution from a nearby city (though this can be corrected for with careful sky observations); and most importantly (3) no clouds can be present to distort the photon counts. If these factors are ideal, then the night will be photometric and little or no corrections to the data will need to be performed.

These conditions are required to obtain the most accurate data and some research projects require photometric conditions to produce valid results.

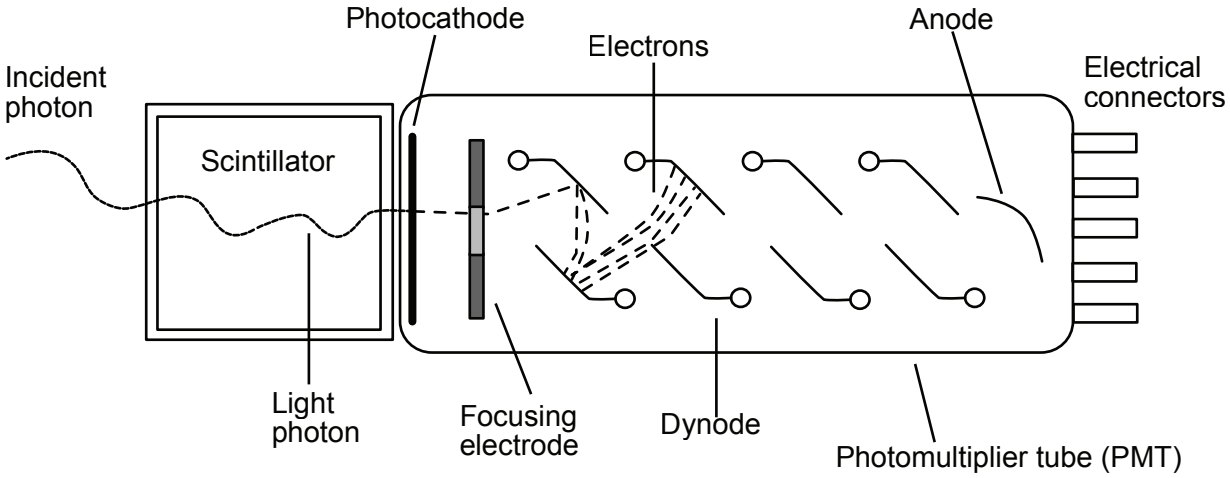

Figure 2.6: Diagram explaining how the photomultiplier works. The incident photon strikes the photocathode creating an electron by the photoelectric effect. This electron proceeds through the tube producing more electrons by secondary emission.

As a result of the electronic revolution, CCDs are now the primary imaging device for most photometric astronomy. These devices are very expensive digital cameras. CCDs have many advantages over older imaging devices. The CCD chip consists of an array of photoelectric light sensors called pixels. The pixel converts the photons into a nearly equal number of electrons and then sends the electrons to a counter. An image is produced by combining the photon counts from each pixel. CCDs have very high quantum efficiency. The SBig STL-1301E (See Fig. 2.7) found on the WMO 16-in telescope has a peak QE of 72%, much better than the 1% QE of the photographic plate. Also, CCDs have a linear response over a very broad spectral range and allow for many objects to be observed simultaneously. (See Fig. 1.1 and Fig. 1.2.) These advantages make the CCD a far better choice over any of the older imaging devices. There are some calibration problems associated with using a CCD as

an imaging device; however, there are standard image processing techniques explained in Section 3.3 that allow raw CCD frames to be corrected.

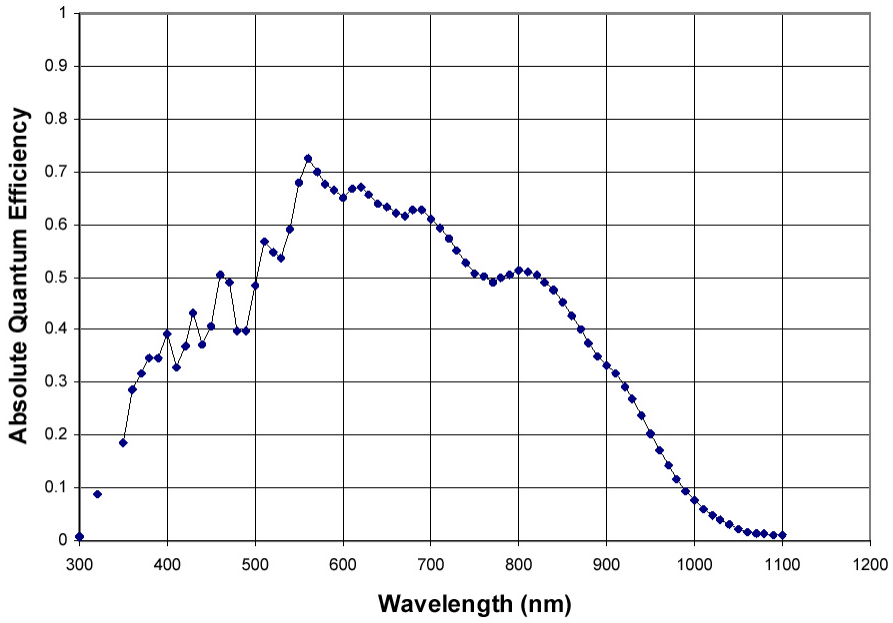

Figure 2.7: The QE according to wavelength of the STL-1301E CCD chip used on the 16-in WMO telescope. SBig (2007).

Chapter 3

Data Reduction and Analysis

3.1 Software

The need for computers and software in astronomy increased dramatically with the invention of the CCD. The electronic images obtained by CCDs are processed and manipulated with computers and software. The most standard software program used in astronomy is known as the Image Reduction and Analysis Facility (IRAF). IRAF provides data analysis packages for the most widely used techniques. The following sections will discuss some techniques for data analysis that are performed in IRAF, including header editing, data reduction, aperture photometry, and an external program called Varstar used to obtain differential magnitudes and the observed Heliocentric Julian Date (HJD).

Other programs are used in conjunction with IRAF to allow for more specific analysis. DS9 is an image manipulation program that can display an image and allow graphical manipulation. This becomes important during aperture photometry when selecting the stars that will be analyzed. Microsoft Excel is used to analyze the variable star period and, together with Maple 10.0, determine the times of maximum light by calculating a least squares fit to Varstar data and taking the zero points of the derivatives. Once these times are considered, we can calculate the difference between the observed times of maximum light and what the calculated times are according to past data (Observed-Calculated or O-C). This difference will help us to determine if the period is changing and calculate the rate of change, if one exists. Final data analysis consists of Fourier decomposition to identify the fundamental periods and their associated frequencies and amplitudes that comprise the light curve of AE UMa. The tool used to produce the Fourier decomposition is Period04. This is a program

from the University of Vienna designed to analyze multi-periodic behavior in unevenly spaced data sets.

3.2 Editing the Image Headers

Astronomers use a wide variety of telescopes, cameras, and software to take stellar images. The software is written by many different companies and the protocols have not been standardized within the field. When a picture is taken, certain information is attached to it. The most important information includes the time of observation (time-obs), date (date-obs), filter type (also known as subset), right ascension, declination, epoch, airmass (amount of atmosphere incoming light must penetrate), and image type (object, zero, flat, dark). These values are found in the image file header.

Often the information in the header is found in a different format than that used in IRAF and Varstar. This means that the header information needs to be edited and formatted to work with the analysis software. For example, the filter is usually labeled "Filter" by the telescope imaging software, but IRAF uses the field "Subset" for that information. More information must also be added. The universal time (UT) is recorded with the observation and the sidereal time (ST) needs to be calculated from the time-obs, date-obs, and observatory location–specifically the longitude. This means that the observatory location must be added to the image headers before the sidereal time is calculated.

This editing must be done before any reduction or analysis can be performed on the image. If this is not accomplished, one of our most important measurements – the times of maximum light – will be incorrect. This would yield incorrect O-C values which would ruin any period calculations.

3.3 Processing Raw CCD Images

CCDs are electronic imaging devices. Therefore, certain problems are inherent to the images produced due to working limitations of the electronic equipment. The

facts that photon counts from stars are converted into electrons and the electronic equipment is powered by electrons give a bit of a challenge to keep an accounting of which electrons come from the different sources. The process for eliminating these problems is called "data reduction." There are three common electronic limitations that must be corrected in every object frame. Correcting a frame is most easily done with other images. In astronomy, the object frames are corrected using calibration frames or images. There are three calibration frames to fix each of the three electronic limitations: bias (or zero) frames, dark frames, and flat frames.

Bias Frames

Bias frames, also known as zero frames, are used to correct an image for electrons that inherently reside in the electronic system. These electrons exist whether or not an image is being taken. This means that electrons are naturally present in some of the CCD wells. This limitation is not dependent on exposure time (also known as integration time), so a bias frame is produced with zero integration time. In other words, it is an instantaneous count of electrons in the un-exposed wells. Many bias frames are taken and averaged together. The final, averaged bias frame is subtracted from the electron count of the data images. This process is performed on every data image collected by the telescopes.

Dark Frames

The dark frames are a count of the number of electrons in the CCD wells that come from thermal noise. This noise may trigger counts during the exposure time that do not come from photons. These images are taken with the shutter closed, hence the name "dark frames." This limitation depends on exposure time and temperature. Therefore, this requires that there be dark frames exposed for the same amount of time that the object being observed will be exposed. If several different objects with different exposure times are observed in one night, several dark frames of different exposure times would be necessary for correct image reduction, unless it is found that

the dark counts scale linearly. The ideal operating temperature for a CCD is very low in order to limit the number of thermal electron emissions in the wells. This temperature is at least $-20°C$ for most CCDs. This kind of temperature is usually reached with thermoelectric cooling systems. Much lower temperatures around $-90°C$ can be reached using liquid nitrogen cooling systems. For each exposure time, all of the dark frames are averaged and combined to form a master dark frame just like the bias frames. This image is then subtracted from all the data images.

Flat Frames

Finally, the flat frame is used to correct for the fact that different pixels respond differently to the incoming light, even if that light is uniform. For this reason, a uniform, or flat, light field is exposed to the CCD in order to get a calibration frame that maps out the pixel sensitivity. The common way for obtaining a uniformly lit field is to take an image of the evening sky at dusk. The sky cannot be too bright or even a very short exposure time like 0.1 seconds will be over-exposed. However, it is best if the sky is not so dim that individual stars are seen, making the field non-uniform. If some stars appear on the flat frames, they will not ruin the flat frames if the telescope is moved after each frame so that the stars will be considered an anomaly and ignored in the flat combine process. The flat frame limitation is dependent on the type of filter used. Therefore, there must be a separate set of flat frames for each filter type used during the observing run. Each set of flat frames are averaged and combined similar to the other calibration frames.

The combined flat frame is a map of how each pixel responds to the light. The most sensitive pixel corresponds to a normalized maximum in the flat frame. Each pixel is sensitive to a percentage of the maximum down to the least sensitive pixel. The combined flat frames are divided into the object frames, according to the type of filter used, to adjust for these different sensitivities.

Once the three calibration frames have been applied to each of the data images, it is possible to perform aperture photometry and extract instrumental magnitudes.

3.4 Aperture Photometry

Aperture photometry (apphot) is a package in IRAF that is used to measure the magnitude of stars in an image. Obtaining the magnitude is the most important part of our data collection. Processing an image to obtain stellar magnitudes is called "photing" an image.

After all the images obtained on a particular night have been corrected using the techniques in Section 3.3, each image can be photed. First, an image is displayed in DS9 and individual stars are selected. In this research we selected AE UMa and five surrounding stars. (See Fig. 1.1 and Fig. 1.2.) Once the stars are selected and the indicators are centered on the stars, a region file is saved that holds the (x,y) coordinates of each star relative to the image's top left corner. This region file also contains numbers designating the order in which the stars were selected. It is used by the apphot package in IRAF to locate the stars on each image. The region file must be re-centered on the stars every frame or two, because the telescopes do not keep the star field in the exact same place as the stars move across the sky.

In order to phot an image there are a few things that need to be done to the configuration files of the apphot package, namely, the circular aperture radius and sky annulus must be set. The aperture is centered on the star based on the coordinates supplied by the coordinate file. The aperture designates how much area or how many pixels should be included in the stellar photon count. This is not an easy choice because the boundary between the star and the sky is not a distinct circle; instead, the photon count falls off from the star's center on a curve similar to a gaussian (See Fig. 3.1). The background sky around the star will also show a photon count that must be subtracted from the photon count inside the aperture to obtain a stellar photon count. This is the function of the sky annulus.

Determining the radius for the aperture and annulus is done by analyzing a radial profile of the photon count from the center of the star to its fringes, as in Fig. 3.1. The important value in the plot is the Half Width at Half Maximum

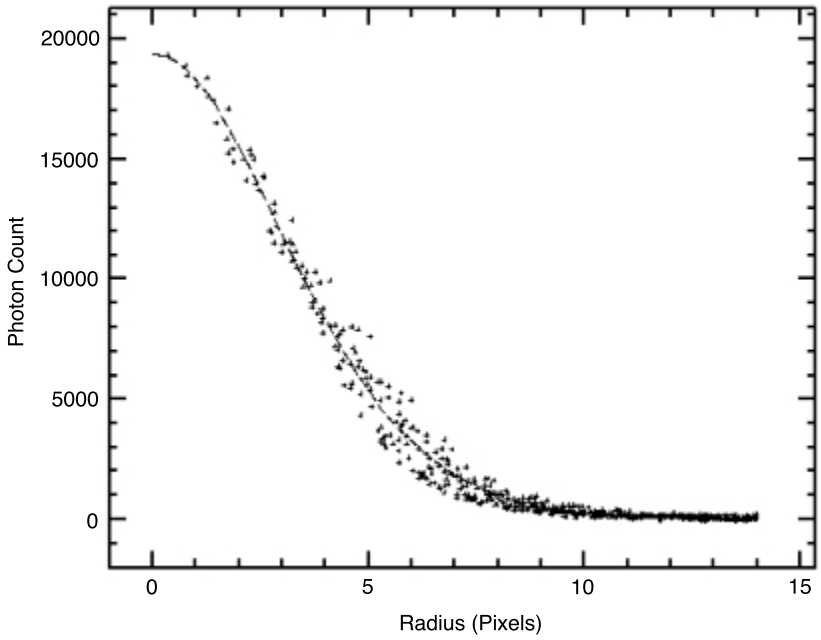

Figure 3.1: Radial profile of AE UMa showing a HWHM of approximately 3.5 pixels while the majority of star light is within 6 pixels.

(HWHM). It is the radius at which the plot drops down to half of the maximum value. In Fig. 3.1 it is approximately 3.5. This value represents the best signal to noise ratio. Most of the star light is found within six pixels of the center, which gives a good value for the aperture radius for this image. The number of pixels containing most of the star light can change from night to night. This is called "seeing." Seeing is a measure of how distorted objects become from atmospheric effects such as air movement. When the seeing is really bad, most of the star light might fit within 10 pixels. When the seeing is really good, most of the light might fit within four pixels. It is important to use an aperture radius that will be large enough to fit the star with the worst seeing out of the five selected stars in the field. For this research we chose an aperture radius of nine. To make very accurate data the aperture radius should be adjusted every frame to correct for the change in seeing conditions.

The annulus has two radii, the outer and inner radii. The annulus' inner radius is generally equal to the aperture radius, while the outer radius is a few pixels larger. For this research an aperture radius of nine pixels, annulus inner radius of 10 pixels, and annulus outer radius of 13 pixels were used. The annulus outer radius is determined by the annulus width which, for this research, was three pixels wide measured from the inner radius outward.

IRAF uses the sky count per pixel obtained from the annulus and subtracts that from each pixel within the aperture. This gives an accurate measure of the stellar photon count. The total number of stellar photons is divided by the exposure time of the image to get the flux *f*, which is the photon count per second from the star. IRAF calculates the magnitude of the star using equation 3.1,

$$m = -2.5 \log_{10} f + C \tag{3.1}$$

where m is the star's apparent magnitude, which is the magnitude seen by an observer. C is an arbitrary constant. For this research we chose a constant of 20. The magnitude is more positive for fainter stars and less positive or more negative for brighter stars.

3.5 Varstar

Varstar is a program written by Dr. Eric Hintz at BYU. This program uses information extracted from the output files, called "mag" files, of apphot. The extracted information includes the star ID (which is the order number from the coordinate file, 1-6 for this research), magnitude, observational time, airmass, and filter. Varstar calculates differential magnitudes for the primary star, AE UMa in this case, and the comparison stars. These magnitudes are independent of temporary observational conditions because it is assumed that if the entire field is dimmed for some reason, the change experienced by one star in the field will be the same for all the field stars. That is the purpose of differential work. It does not require photometric conditions.

The differential magnitude is a measure of the magnitude difference between an ensemble average magnitude and each star's magnitude. Varstar prints the magnitudes on the screen along with the calculated error associated with determining the average magnitude of each star. Stars with large errors are those that have had significant fluctuations in their magnitude. AE UMa produces the largest error, but is not the only large error star in the field. Out of the six stars that we used, three of them were maintained as comparison stars. They are stars 3, 4, and 6 in Fig. 1.1. AE UMa and stars 2 and 5 showed larger errors. After eliminating the high-error stars, Varstar creates an ensemble of the stable stars for comparison and averages their magnitudes. Varstar calculates the differential magnitudes by taking the difference between the average ensemble magnitude of the stable stars and the magnitude of each individual star. These differential magnitudes are output along with the HJD to a separate data file for each of the six stars. Varstar's output files contain the data necessary to obtain the times of maximum light. Fig. 3.2 shows a plot of the Varstar data file for AE UMa on May 9, 2007 from the WMO 12-in telescope.

Once data points are plotted in Varstar, it becomes very apparent that some of the points do not fit with the rest of the data. These "flier" points are observations that, for one reason or another, are bad. It is possible that the electronics malfunctioned or that some anomaly in the sky caused the measurements to be high or low. No matter the cause, these data points have to be systematically removed from the Varstar data. This can be done by pinpointing the approximate time (HJD) of the bad data point on the graph and locating it in the data file. In the data file, each differential magnitude differs from the previous one by only a few milli-magnitudes, or thousandths of a magnitude. When a flier point is located it is fairly easy to determine which line it is in the data file because its magnitude differs from those around it by hundredths of a magnitude or more. Once this data point is removed from the file, the plot can be made again and more accurate trends can be applied to the graphs.

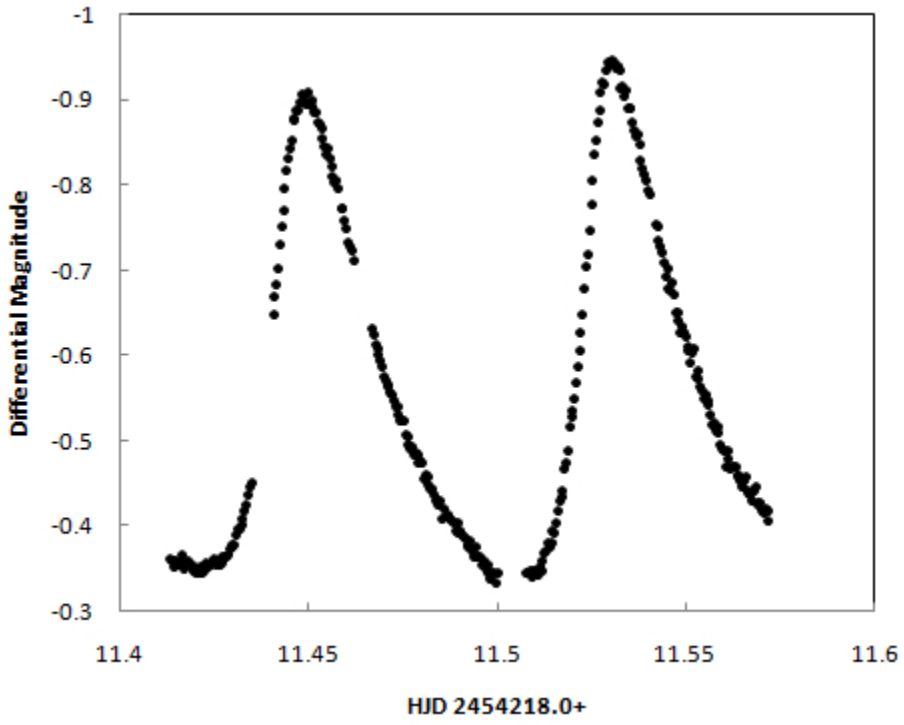

Figure 3.2: The variable light curve of AE UMa recorded on May 9, 2007 .

3.6 Obtaining Times of Maximum Light

The Varstar output plotted in Fig. 3.2 can be used to determine the time of maximum light to a fairly accurate level. To do this, data from the Varstar output file for the variable star is imported into a spreadsheet program (we used Microsoft Excel). Once imported, the data points surrounding the times of maximum light can be plotted to form an upside-down parabola seen in Fig. 3.3. A third order polynomial can be fitted to this curve by the least squares method. This method finds the line that minimizes the sum of the squares of the errors of each point from the line. The time at which the derivative of the fitted polynomial equals zero is the time of maximum light.

Maple 10.0 is a program that makes it easy to take the derivative of a polynomial and solve for the zero point. In order to do this with satisfactory accuracy the Varstar output data needed to be edited. Because the fitted polynomial from Excel

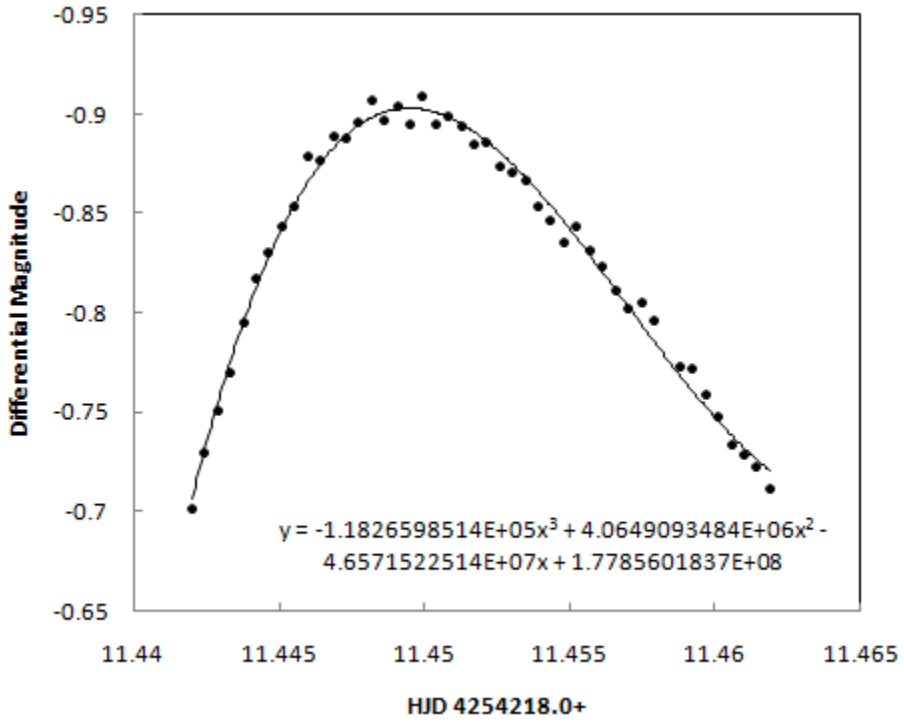

Figure 3.3: The variable light curve of AE UMa around the time of maximum light.

uses large exponents, the HJD of the Varstar data needed to be reduced from four significant digits before the decimal point to two significant figures (Varstar leaves off the first three significant digits of the HJD–2450000.0+ in this research). To do this we found the oldest observational HJD in Varstar, which was 4218.0+. This number was subtracted from the HJD of all observations to obtain HJDs of 2454218.0+. For example, if Varstar reported an HJD of 4218.4536 then the modified HJD used to obtain the time of maximum light was $4218.4536 - 4218 = 0.4536$.

3.7 Calculating Cycle Number and O-C

Broglia and Conconi (1975) reported a relationship between the HJD of pulsation maxima and the cycle number. This relation is represented by an equation. The zero point used in the equation, known as an epoch, was their first observed time of maximum light. This equation, known as an ephemeris, is reported in their paper:

$$\mathrm{HJD}_{max} = 2442062.5823 + 0.086016883 \times E \tag{3.2}$$

HJD_{max} is the time of maximum light and the cycle number (E) is how many maximums have passed since the zero point maximum in 1974. With this equation the cycle number for the times of maximum light that we have observed can be calculated by substituting our HJDs of maximum light into Eq. 3.2. These cycle numbers are not usually whole numbers due to measurement limitations. Therefore, the cycle numbers are rounded to the nearest whole number. Once the cycle number is obtained, it can be backward substituted into the ephemeris to obtain a calculated time of maximum.

An important value for determining the period change in a variable star is called the O-C value. The name "O-C" comes from the words "observed" and "calculated." It is literally the difference between the observed time of maximum and the calculated time of maximum, as described above. The O-C values are small numbers, usually on the order of a 10^{-2} or 10^{-3}. These values can be plotted against their cycle numbers or their observed HJDs. When these values are plotted, a trend can be seen in the data and a line can be fit. An O-C diagram for all observed cycles since 1974 is shown in Fig. 3.4.

The linear fit of the data is an indication that the period has stayed fairly constant over the past 33 years. However, a more rigorous statistical analysis will need to be performed to determine if a curve can reasonably be fit to the data instead. The fact that the line has a slope of 1.926×10^{-7}, as indicated by the equation in Fig. 3.4, shows that the initial period used in Eq. 3.2 of $P_0 = 0.086016883$ is incorrect by the slope value. To correct for this, a new ephemeris was calculated:

$$\mathrm{HJD}_{max} = 2442062.5823 + 0.086016883 \times E + (1.926 \times 10^{-7} \pm 3.1 \times 10^{-9}) \times E \tag{3.3}$$

This period-corrected ephemeris yields a new period of $P_0 = 0.0860170756 \pm 3.1 \times 10^{-9}$. From this new ephemeris we calculated a period-corrected HJD. This

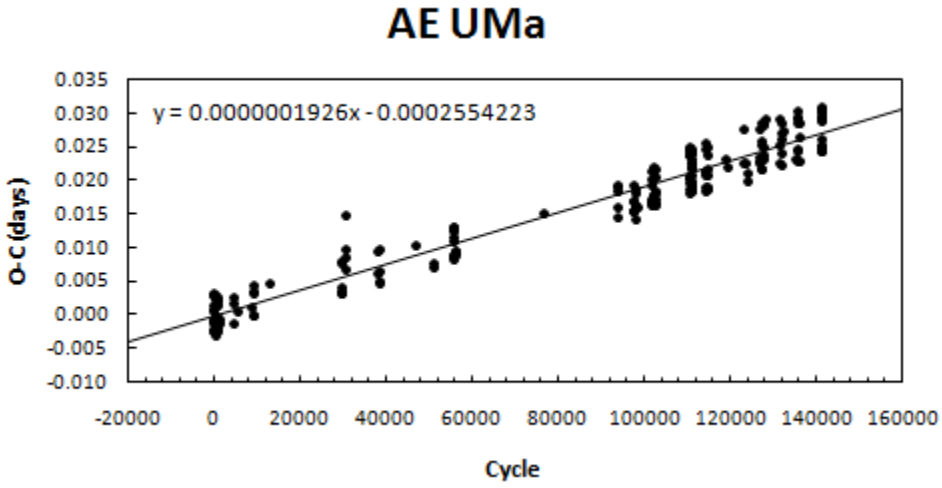

Figure 3.4: The O-C diagram for all the observed maxima of AE UMa from 1974 to the present. The trendline fit is easily linear but with a slope, indicating an inaccurate period in Eq. 3.2.

HJD was used to obtain period-corrected O-C values and those values are plotted with cycle number in Fig. 3.5.

The linear trendline in Fig. 3.5 crosses the O-C axis at approximately -0.00025. This is an indication that the original epoch of 2442062.5823 used in Eq. 3.2 and Eq. 3.3 is inaccurate. To correct this, the O-C axis intercept needed to be subtracted from the old epoch, yielding a new epoch of $2442062.58205 \pm 0.00032$. This process gives us a better looking epoch from our reference point. However, the epoch error was 0.00032, which is actually greater than our epoch correction of 0.00025. This means that this epoch correction is statistically unnecessary, but we made the correction for data aesthetics. This resulted in the final ephemeris that is corrected for both period and epoch inaccuracies:

$$\mathrm{HJD}_{max} = 2442062.5823 - (0.00025 \pm 0.00032) + 0.086016883 \times E + (1.926 \times 10^{-7} \pm 3.1 \times 10^{-9}) \times E \tag{3.4}$$

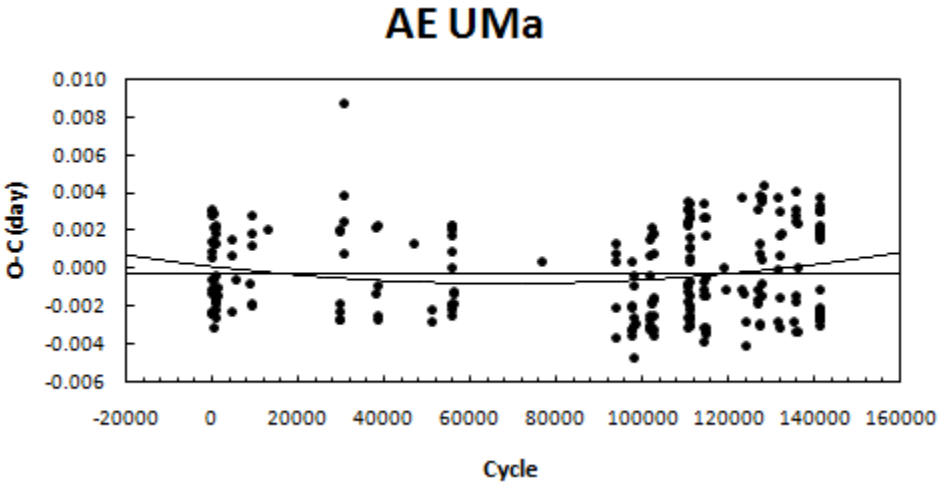

Figure 3.5: The period-corrected O-C diagram for all the observed maxima of AE UMa from 1974 to the present. The linear trendline now has no slope, indicating an accurate period $P_0 = 0.0860170756 \pm 3.1 \times 10^{-9}$. The linear trendline, however, crosses the y-axis at -0.00025, indicating an inaccurate epoch in the ephemeris.

New HJDs and O-C values were calculated from this corrected ephemeris and plotted with cycle number in Fig. 3.6. A linear trend is evidence for no period change, while a curved trend is evidence for a very small period change. The more curved the line is, the greater the period change. If the convex parabola in Fig. 3.6 is a good fit for this data, this would indicate a slowly increasing period, or in other words, a longer time span between consecutive times of maximum light. This data refutes the conclusions made by Hintz et al. (1997) that the period change was decreasing at the fast rate of $-1.14 \times 10^{-10} dd^{-1}$. Equation 3.5, represents the quadratic fit in Fig. 3.6.

$$y = 1.94623 \times 10^{-13} x^2 - 2.6290223 \times 10^{-8} x + 3.512537 \times 10^{-4} \qquad (3.5)$$

The coefficient error for the quadratic term in this trendline equation is 9.03219×10^{-14}, which is 2.15 times smaller than the coefficient itself. This creates the possibility that the primary period of AE UMa is increasing very slowly. To make a definitive case for this behavior, more data over a longer time period is needed.

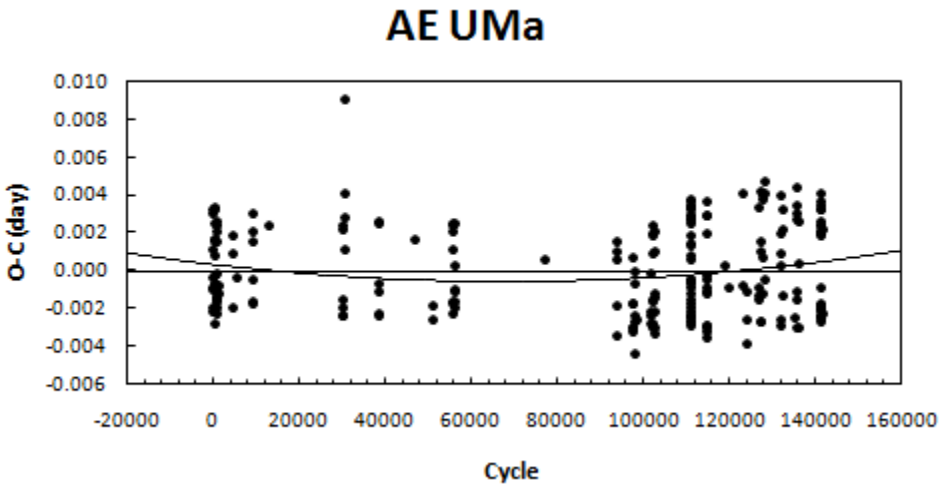

Figure 3.6: The epoch and period-corrected O-C diagram for all the observed maxima of AE UMa from 1974 to the present. There is a possibility to fit a curve to this data, which would indicate a period change.

3.8 Fourier Analysis and the First Harmonic

Fourier analysis consists of decomposing a signal wave into its fundamental components. This can be done on any sort of periodic wave, from sound waves to the light curves formed by the pulsation of AE UMa. Successful Fourier analysis produces the frequencies, amplitudes and phases associated with the fundamental waves comprising the final wave form. In our case there will be a frequency associated with the fundamental period and any overtone or harmonic waves apart from the fundamental. It was expected that overtone frequencies will exist because the light curves from AE UMa do not form a simple sine wave.

Using Period04, we were able to import a data string containing 3562 points of differential magnitudes and their corresponding HJDs. This data string was composed of V filter data from WMO, OPO and Tenagra. Some of the data were not used in this Fourier analysis because of various reasons that will be explained in the next section.

Once the data were imported into Period04, it was processed using Fourier analysis. This type of analysis breaks down a complex waveform into many fundamental sine waves of various frequencies, amplitudes, and phases. This is done by taking the Fourier transform of the function representing the time based data string to produce a function representing the frequencies of the time-series. The Fourier transform is represented by the equation:

$$F(\nu) = \int f(t) \exp^{i2\pi\nu t} \, dt \tag{3.6}$$

From this equation a power spectrum was obtained comparing the frequencies with their amplitudes in Fig. 3.7. This graph shows the fundamental frequency associated with the primary period P_0 at about $f_0 = 11.63$. The peak of the second, small hump represents a multiplicity of the fundamental frequency at $2f_0$.

Once this primary frequency and amplitude were calculated from the power spectrum, the phase was calculated using a least-squares solution. Equation 3.7 is the formula used to calculate the line of best fit using a least-squares solution.

$$\Delta m = a_0 + \sum_{i,j} a_{i,j} sin(2\pi f_{i,j} + \varphi_{i,j}) \tag{3.7}$$

After the fundamental frequency was calculated, the first overtone frequency f_1 was obtained by subtracting the effect of the primary frequency f_0 out of the power spectrum. This revealed the next biggest component in the power spectrum, which happened to be $2f_0$=23.2511556. This was subtracted out of the power spectrum and the next frequency obtained was the first overtone $f_1 = 15.0315332$, which corresponds to the period in Equation 3.8.

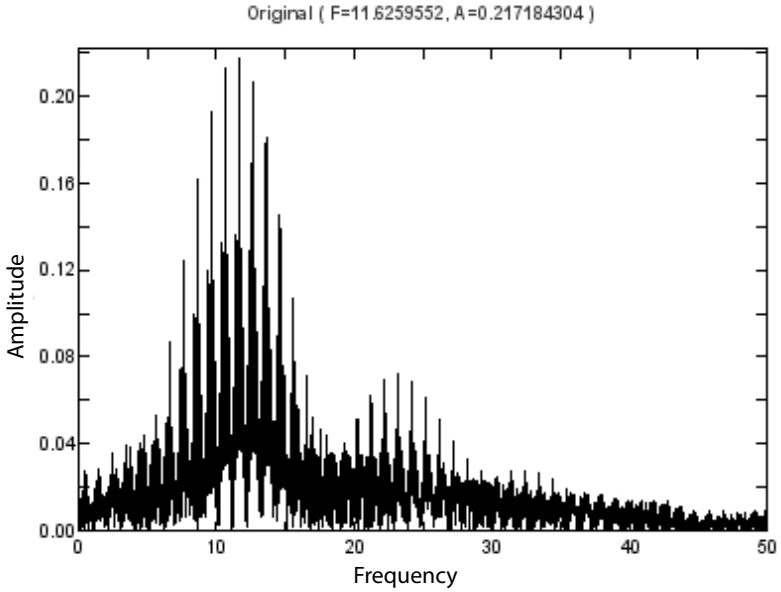

Figure 3.7: Fourier plot from the V filter data acquired in 2007. Notice that the frequency with the maximum amplitude lies at 11.62 and corresponds to the frequency of the primary period P_0.

$$P_1 = 1/f_1 = 0^d.066529 \tag{3.8}$$

Repeating this process after each frequency led us to linear combinations of the primary and first harmonic frequencies, according to Equation 3.9. The complete list of frequencies can be found in Table 3.1. For our purposes we used the constraints $0 \leq i \leq 4$ and $0 \leq j \leq 1$, considering that higher order residuals were not significant.

$$f_{i,j} = |if_0 \pm jf_1| \tag{3.9}$$

The frequency, amplitude, and phase of the frequencies obtained by the Fourier analysis were combined to create the final line of best fit. This line is a reproduction of the light curve of AE UMa. Figure 3.8 shows the data points from the light curve

Table 3.1. Frequencies Within AE UMa's Light Curve

Terms	Frequency	Amplitude	Phase
f_0	11.625720	0.21634996	0.398558
$2f_0$	23.251156	0.07004265	0.377335
f_1	15.031533	0.04187648	0.679528
$3f_0$	34.875842	0.02553788	0.535520
$f_0 + f_1$	26.657099	0.02821727	0.112931
$f_1 - f_0$	3.402257	0.02668300	0.038409
$2f_0 + f_1$	38.282063	0.01491555	0.100538
$4f_0$	46.495759	0.01072621	0.886660

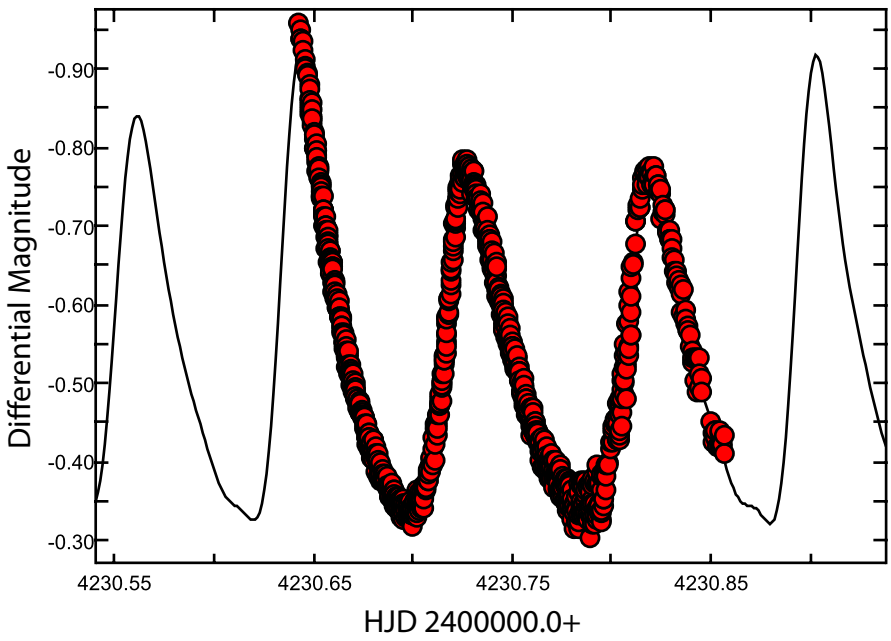

Figure 3.8: Time-String data set superimposed over periodic curve obtained from waves calculated from Fourier analysis.

of AE UMa superimposed over the light curve calculated from the Fourier decomposition. Continuing the Fourier decomposition yields many linear combinations of the primary and first overtone frequencies. This continues to the point of significant error to noise ratios. Therefore, no more independent frequencies were established with our data set.

3.9 Data Corrections

Several problems presented themselves when working with the data from aperture photometry and Varstar. These problems were corrected for and did not have a significant impact on the final results. These problems were observed while trying to calculate the O-C values and while trying to create a valid data set for Period04 Fourier analysis. We found that the WMO data from both the 12 and 16-in telescopes had incorrect HJDs. These values were off by exactly six hours, or 0.25 days. This was easily adjusted for by adding 0.25 to the HJDs from the West Mountain data. The time error was due to the fact that Mountain Daylight Time was recorded instead of Universal Time.

The second problem we encountered was that some of the data from West Mountain was recorded as being in the V filter but was actually acquired in the R filter. Two nights of data from the WMO 12-in telescope were observed strictly in the R filter, which changed the differential magnitudes and light curve amplitudes significantly (see Fig. 3.9). However, the times of maximum light from these curves are very close to those from the 16-in V filter data on the same nights. The three times of maximum that were recorded in the red filter on the WMO 12-in are 2454236.67, 2454236.75 and 2454235.72. These data were not used in the Fourier analysis.

The third problem we found was that the data from the OPO containing two maximums at 2454244.67 and 2454244.76 seems to be offset in zero point from any other V light curves recorded in this investigation. The most likely cause for the shift in differential magnitudes comes from a problem with the photometry performed on this data set, or the Varstar calculations. Though the magnitudes change a lot,

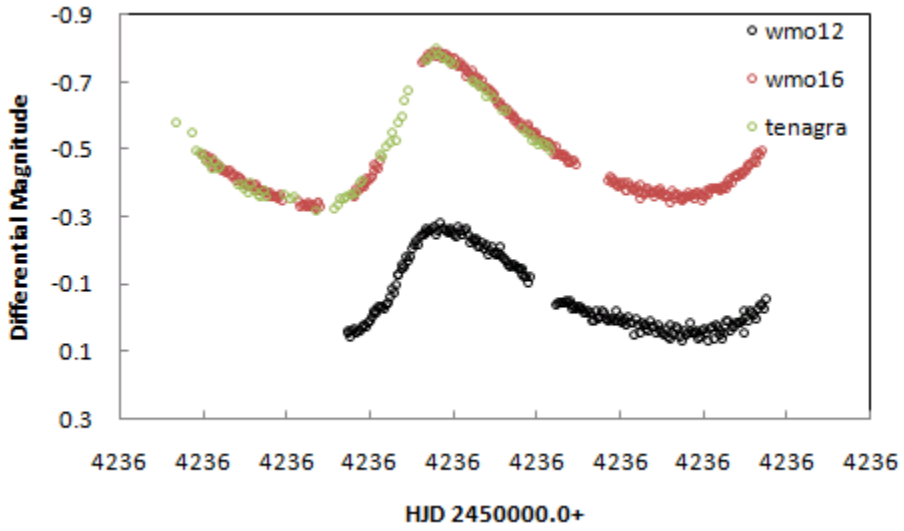

Figure 3.9: During this observing run the WMO 12 inch was using the R filter rather than the expected V filter.

the times of maximum light seem to fit the equations giving very reasonable O-C values. For this reason we included the times of maximum from this data set in this research but, did not include this night in the Fourier analysis because of the zero point shift. Further investigation proved that the Varstar calculations were correct making aperture photometry the likely source for the data shift.

Finally, one observing night on the WMO 16-in produced a light curve that provided an accurate time of maximum light, but the amplitude of the curve was much smaller than expected. The odd part about this curve is that the maximum differential magnitude is equal to that for the 12-in V filter data on the same night. The reason for this discrepancy is that the wrong comparison stars were used in the Varstar calculations. This produced incorrect differential magnitudes that were easily corrected by running the data through Varstar with the correct comparison stars. Once this correction was made, the time of maximum was recalculated and the data string was added to the Fourier analysis. This changed the frequencies, amplitudes and phases; however, the change was not significant. The time of maximum recorded with this light curve is 2454246.73.

Chapter 4

Results and Conclusions

4.1 The Multi-Periodicity of AE UMa

The purpose of this paper was to determine what the period of AE Uma has been doing since the star was discovered to be a variable star. The first measurements taken on this star were photographic and visual (See Table A.1). These measurements were key to determining the variability of AE UMa; however, they are not reliable data points for statistical analysis. Therefore, in the final data analysis these data points were not considered. The final ephemeris (see Eq. 3.4) has corrected values for the epoch and period which are $2442062.58205 \pm 0.00032$ and $P_0 = 0^d.0860170756 \pm 3.1 \times 10^{-9}$, respectively. Fourier analysis led to the the primary frequency $f_0 = 11.625$, which is different from the observed frequency of 11.6255987. The first overtone frequency $f_1 = 15.031$, corresponding to a period $P_1 = 0^d.0665291730$, was also obtained through the Fourier analysis.

The trendlines established in Fig. 3.6 indicated that though there is the possibility for a period increase over the past 33 years, the zero slope on the linear trendline shows that the period has not made any significant change over this long time period. The coefficient error for the quadratic fit has a T value of 2.15, which makes this a marginal possibility for a good data fit. Rigorous statistical analysis and a larger data set would perhaps yield evidence to accept and calculate a possible period increase

As mentioned in the introduction, this research is a follow-up to the paper written by Hintz et al. (1997). The data presented in this research agree with that presented by Pócs & Szeidl (2001) and Zhou (2001). The period of AE UMa is not decreasing but rather seems to be relatively unchanging over the past 33 years. Taking a closer look at the O-C data in Fig. 4.1, it is clear that the 1997 data set is relatively low on the O-C scale. This would result in a data set average much lower than the

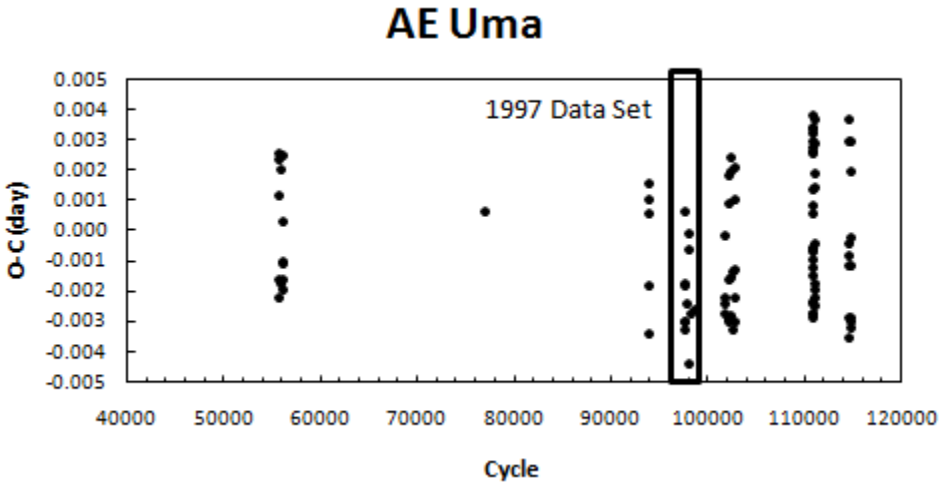

Figure 4.1: The O-C data from 1997 is highlighted. The entire data set is low on the O-C diagram so the average would be low in Fig. 3 from Hintz et al. (1997). This would make it appear that the period was decreasing.

previous set and an upside down parabola would be suggested, indicating a quickly decreasing period.

4.2 Conclusion

Each time a paper is published on AE UMa, the results get increasingly better. Having a long observational history has allowed long term effects to be studied, such as period change. As the star is observed in the future these studies will be able to be more accurate in determining what AE UMa and stars like it are doing and how they are evolving. One basis for stellar research is to prove or disprove the accuracy of current evolutionary models. Since stellar evolution occurs over billions of years, it is difficult to measure many effects on a short time scale. This is why observation of the same objects over many, many years is the only way to test theoretical models.

According to current stellar evolutionary theories, as a star ages it increases in size, thereby making it more luminous. This would affect the period by making it longer. So in theory, the period of AE UMa should increase over time if evolutionary effects are the only factors governing the radial pulsation. If this is not the case, then

one of two things are possible: (1) the stellar evolutionary models are not correct and need to be modified; or (2) the pulsation of stars like AE UMa does not depend on stellar evolution but on some internal process or processes not yet understood. Either way, the more these stars are studied, the more we will be able to determine about how stars live, breathe, and die.

Appendix A

Times of Maximum Light

Table A.1. Times of Maximum Light for AE Ursae Majoris

Year	HJD_{max}*	Det.	Cycle	O-C	Source	Year	HJD_{max}*	Det.	Cycle	O-C	Source
1937	28632.3980	pg	-156134	0.0060	1		50899.3729	CCD	102733	-0.0013	3
1946	31875.1220	pg	-118436	-0.0277	2		50899.4570	CCD	102734	-0.0033	3
1950	33379.2560	pg	-100949	0.0117	2		50902.2976	CCD	102767	-0.0012	3
1956	35601.1880	pg	-75118	0.0366	2		50902.3819	CCD	102768	-0.0029	3
	35604.3370	vis	-75081	0.0030	1		50903.3321	CCD	102779	0.0011	3
	35607.1730	pg	-75048	0.0004	2		50903.4192	CCD	102780	0.0022	3
1957	35981.2020	pg	-70700	0.0272	2		50903.5009	CCD	102781	-0.0022	3
1963	38106.4020	vis	-45993	0.0033	1	2000	51608.0716	CCD	110972	0.0027	12
1971	41059.3680	vis	-11663	0.0031	1		51608.1577	CCD	110973	0.0028	12
1973	41773.2230	vis	-3364	0.0024	1		51608.2395	CCD	110974	-0.0014	12
1974	42062.5832	pm	0	0.0012	3		51608.3264	CCD	110975	-0.0006	12
	42065.5959	pm	35	0.0033	4		51609.0186	CCD	110983	0.0035	12
	42065.6778	pm	36	-0.0009	4		51609.1007	CCD	110984	-0.0005	12
	42068.3432	pm	67	-0.0020	4		51609.1865	CCD	110985	-0.0007	12
	42068.4302	pm	68	-0.0010	4		51609.2770	CCD	110986	0.0038	12
	42068.5203	pm	69	0.0031	4		51609.3583	CCD	110987	-0.0009	12
	42068.6029	pm	70	-0.0003	4		51610.0450	CCD	110995	-0.0023	12
	42068.6871	pm	71	-0.0022	4		51610.9969	CCD	111006	0.0034	12
	42069.3808	pm	79	0.0034	4		51611.0821	CCD	111007	0.0026	12
	42069.4651	pm	80	0.0017	4		51611.1627	CCD	111008	-0.0028	12
	42069.5473	pm	81	-0.0021	4		51612.0246	CCD	111018	-0.0011	12
	42069.6363	pm	82	0.0008	4		51612.1091	CCD	111019	-0.0027	12
	42086.4965	pm	278	0.0017	4		51612.2010	CCD	111020	0.0033	12
	42086.5787	pm	279	-0.0021	4		51612.2846	CCD	111021	0.0009	12
	42087.4390	pm	289	-0.0020	4		51612.3704	CCD	111022	0.0006	12
	42087.5263	pm	290	-0.0007	4		51612.9692	CCD	111029	-0.0027	12
	42087.6155	pm	291	0.0025	4		51613.0609	CCD	111030	0.0030	12
	42095.5298	pm	383	0.0032	3		51613.1453	CCD	111031	0.0014	12
	42095.6123	pm	384	-0.0003	3		51613.2276	CCD	111032	-0.0023	12
	42103.3513	pm	474	-0.0028	4		51613.3156	CCD	111033	-0.0004	12
	42106.4523	pm	510	0.0015	3		51615.0341	CCD	111053	-0.0022	12
	42119.5252	pm	662	-0.0002	3		51615.1260	CCD	111054	0.0037	12
	42121.5025	pm	685	-0.0012	3		51615.2098	CCD	111055	0.0015	12
	42122.3628	pm	695	-0.0011	4		51615.2919	CCD	111056	-0.0024	12
	42122.4484	pm	696	-0.0015	4		51615.9855	CCD	111064	0.0030	12

Table A.1 (continued)

Year	HJD_{max}*	Det.	Cycle	O-C	Source	Year	HJD_{max}*	Det.	Cycle	O-C	Source
	42128.2968	pm	764	-0.0023	3		51616.0705	CCD	111065	0.0020	12
	42128.3872	pm	765	0.0021	3		51616.1526	CCD	111066	-0.0019	12
	42128.4727	pm	766	0.0016	3		51616.2388	CCD	111067	-0.0017	12
	42128.5557	pm	767	-0.0014	3	2001	51929.2556	CCD	114706	-0.0011	12
	42133.4627	pm	824	0.0026	3		51929.3464	CCD	114707	0.0037	12
	42133.5442	pm	825	-0.0019	3		51930.2059	CCD	114717	0.0030	12
	42134.4055	pm	835	-0.0008	3		51930.2885	CCD	114718	-0.0004	12
	42147.3933	pm	986	-0.0016	3		51930.3721	CCD	114719	-0.0029	12
	42148.4295	pm	998	0.0024	3		51931.2316	CCD	114729	-0.0035	12
	42148.5117	pm	999	-0.0014	3		51931.3203	CCD	114730	-0.0008	12
	42159.4365	pm	1126	-0.0008	3		51941.2102	CCD	114845	-0.0029	12
	42161.4145	pm	1149	-0.0012	3		51941.2979	CCD	114846	-0.0011	12
1975	42453.5306	pm	4545	0.0009	3		51941.3881	CCD	114847	0.0030	12
	42453.6137	pm	4546	-0.0020	3		51942.1563	CCD	114856	-0.0030	12
	42460.4989	pm	4626	0.0019	3		51942.2473	CCD	114857	0.0020	12
	42532.4070	vis	5462	-0.0003	5		51942.3311	CCD	114858	-0.0002	12
1976	42830.6280	pm	8929	-0.0005	3		51942.4141	CCD	114859	-0.0032	12
	42837.5120	pm	9009	0.0021	3	2002	52321.4089	CCD	119265	0.0004	13
	42838.4591	pm	9020	0.0030	3		52371.3836	CCD	119846	-0.0009	13
	42866.4960	vis	9346	-0.0016	5	2003	52685.3460	CCD	123496	-0.0008	13
	42869.3377	pm	9379	0.0015	3		52685.4369	CCD	123497	0.0041	13
	42869.4205	pm	9380	-0.0017	3		52730.4187	CCD	124020	-0.0010	13
1977	43162.5708	pm	12788	0.0024	3		52739.3617	CCD	124124	-0.0038	13
1981	44633.4626	pm	29888	0.0022	3		52745.4702	CCD	124195	-0.0025	14
	44633.5440	pm	29889	-0.0024	3		52980.5608	CCD	126928	0.0034	15
	44633.6309	pm	29890	-0.0015	3		52980.6421	CCD	126929	-0.0013	15
	44634.4046	pm	29899	-0.0020	3		52980.7279	CCD	126930	-0.0015	15
	44634.4902	pm	29900	-0.0024	3		53003.5231	CCD	127195	-0.0008	14
	44634.5810	pm	29901	0.0024	3	2004	53028.2942	CCD	127483	-0.0027	14
	44692.4709	pm	30574	0.0028	3		53028.3871	CCD	127484	0.0042	14
	44696.3430	vis	30619	0.0041	6		53028.4705	CCD	127485	0.0016	14
	44696.4260	vis	30620	0.0011	6		53028.5522	CCD	127486	-0.0027	14
	44696.5200	vis	30621	0.0091	6		53028.6420	CCD	127487	0.0011	14
1983	45355.4902	pm	38282	0.0025	3		53069.4119	CCD	127961	-0.0011	14
	45355.5727	pm	38283	-0.0010	3		53069.5029	CCD	127962	0.0039	14

Table A.1 (continued)

Year	HJD$_{max}$*	Det.	Cycle	O-C	Source	Year	HJD$_{max}$*	Det.	Cycle	O-C	Source
	45382.3228	pm	38594	-0.0023	3		53070.4493	CCD	127973	0.0041	14
	45382.4104	pm	38595	-0.0007	3		53070.5320	CCD	127974	0.0008	14
	45382.4997	pm	38596	0.0026	3		53090.4053	CCD	128205	0.0041	14
	45382.5807	pm	38597	-0.0024	3		53094.3575	CCD	128251	-0.0005	14
1985	46114.3320	vis	47104	0.0016	7		53110.3619	CCD	128437	0.0047	16
1986	46468.4601	pm	51221	-0.0026	3	2005	53409.5286	CCD	131915	0.0040	17
	46468.5468	pm	51222	-0.0019	3		53409.6108	CCD	131916	0.0003	17
1987	46855.6279	pm	55722	0.0024	8		53409.6941	CCD	131917	-0.0025	17
	46856.5729	pm	55733	0.0012	8		53427.3272	CCD	132122	-0.0029	16
	46856.6561	pm	55734	-0.0016	8		53427.4181	CCD	132123	0.0020	16
	46857.6017	pm	55745	-0.0022	8		53427.5031	CCD	132124	0.0010	16
	46857.6925	pm	55746	0.0026	8		53451.4136	CCD	132402	-0.0013	16
	46858.6382	pm	55757	0.0021	8		53451.5042	CCD	132403	0.0033	16
	46859.6666	pm	55769	-0.0017	8		53484.3616	CCD	132785	0.0022	16
	46878.4181	pm	55987	-0.0019	8		53716.5170	CCD	135484	-0.0025	18
	46878.5064	pm	55988	0.0003	8	2006	53765.3803	CCD	136052	0.0031	19
	46878.5946	pm	55989	0.0025	8		53765.4660	CCD	136053	0.0028	19
	46884.5262	pm	56058	-0.0011	8		53765.5462	CCD	136054	-0.0030	19
	46884.6117	pm	56059	-0.0016	8		53766.3278	CCD	136063	0.0044	19
	46886.5907	pm	56082	-0.0010	8		53766.4079	CCD	136064	-0.0015	19
1992	48683.3170	pm	76970	0.0007	9		53766.4943	CCD	136065	-0.0011	19
1996	50151.4564	pm	94038	0.0006	3		53766.5849	CCD	136066	0.0035	19
	50151.5384	pm	94039	-0.0034	3		53794.3619	CCD	136389	-0.0030	17
	50152.3170	pm	94048	0.0011	3		53795.3115	CCD	136400	0.0004	17
	50152.4862	pm	94050	-0.0018	3		53795.3998	CCD	136401	0.0027	17
	50152.5756	pm	94051	0.0016	3	2007	54222.7275	CCD	141369	-0.0024	20
1997	50458.8815	CCD	97612	0.0007	10		54223.6743	CCD	141380	-0.0018	20
	50458.9636	CCD	97613	-0.0032	10		54226.6902	CCD	141415	0.0035	20
	50459.8240	CCD	97623	-0.0030	10		54227.7170	CCD	141427	-0.0020	20
	50459.9113	CCD	97624	-0.0017	10		54229.6995	CCD	141450	0.0021	20
	50467.7388	CCD	97715	-0.0018	10		54229.6995	CCD	141450	0.0022	20
	50467.8236	CCD	97716	-0.0030	10		54229.7807	CCD	141451	-0.0027	20
	50490.3607	CCD	97978	-0.0024	3		54230.7271	CCD	141462	-0.0024	20
	50505.6697	CCD	98156	-0.0044	10		54230.7276	CCD	141462	-0.0020	20
	50505.7595	CCD	98157	-0.0006	10		54230.7277	CCD	141462	-0.0018	20

Table A.1 (continued)

Year	HJD_{max}*	Det.	Cycle	O-C	Source	Year	HJD_{max}*	Det.	Cycle	O-C	Source
	50505.8461	CCD	98158	0.0000	10		54230.8192	CCD	141463	0.0037	20
	50516.7676	CCD	98285	-0.0027	10		54231.6790	CCD	141473	0.0033	20
	50554.4432	CCD	98723	-0.0026	3		54234.6888	CCD	141508	0.0024	20
1998	50813.3550	CCD	101733	-0.0022	3		54235.7162	CCD	141520	-0.0024	20
	50813.4408	CCD	101734	-0.0024	3		54235.7165	CCD	141520	-0.0021	20
	50813.6151	CCD	101736	-0.0001	3		54235.7177**	CCD	141520	-0.0008	20
	50813.6985	CCD	101737	-0.0027	3		54236.6674	CCD	141531	0.0026	20
	50848.4540	CCD	102141	0.0019	3		54236.6688**	CCD	141531	0.0041	20
	50848.5391	CCD	102142	0.0009	3		54236.7526**	CCD	141532	0.0019	20
	50848.6212	CCD	102143	-0.0030	3		54236.7528	CCD	141532	0.0021	20
	50849.4815	CCD	102153	-0.0028	3		54237.6952	CCD	141543	-0.0017	20
	50849.5688	CCD	102154	-0.0016	3		54244.6676	CCD	141624	0.0033	20
	50862.3840	CCD	102303	-0.0029	11		54244.7480	CCD	141625	-0.0023	20
	50872.2809	CCD	102418	0.0020	3		54246.7308	CCD	141648	0.0020	20
	50872.3634	CCD	102419	-0.0015	3		54246.7311	CCD	141648	0.0024	20
	50872.4481	CCD	102420	-0.0028	3		54250.6833	CCD	141694	-0.0022	20
	50872.5394	CCD	102421	0.0025	3		54251.7200	CCD	141706	0.0023	20

References. — 1 Tsesevich (1973), 2 Filatov (1960), 3 Pócs & Szeidl (2001), 4 Broglia & Conconi (1975), 5 Braune et al. (1979), 6 Braune & Mundry (1982), 7 Hübscher et al. (1986), 8 Rodríguez et al. (1992), 9 Hübscher et al. (1992), 10 Hintz et al. (1997), 11 Agerer et al. (1999), 12 Zhou (2001), 13 Agerer & Hübscher (2003), 14 Hübscher (2005), 15 Hübscher et al. (2005), 16 Hübscher et al. (2006), 17 Klingenberg et al. (2006), 18 Bíró et al. (2006), 19 Hübscher & Walter (2007), 20 Current Paper.

* The HJD_{max}'s reported in this table are based on the epoch 2400000.0+.

** These times of maximum light were the duplicates taken in the R filter.

References

Agerer, F., Dahm, M., & Hübscher, J. 1999, IBVS, 4712

Agerer, F. & Hübscher, J. 2003, IBVS, 5485

Bessell, M. S. 1979, PASP, 91, 589

Bíró, I. B., Borkovits, T., Csizmadia, S., Hegedüs, T., Klagyivik, P., Kiss, Z. T., Kovács, T., Lampens, P., Patkós, L., Pál, A., Regály, Z., & Van Cauteren, P. 2006, IBVS, 5684

Braune, W., Hübscher, J., & Mundry, E. 1979, Astron. Nachr., 300, 165

Braune, W. & Mundry, E. 1982, BAV Mitt. Nr., 34

Astronomy Research Group at Brigham Young University 2007, (http://astronomy.byu.edu)

Broglia, P. & Conconi, P. 1975, A&AS, 232, 243

Cousins, A. W. J. 1974, MNSSA, 33, 149

Crawford, D. L. & Barnes, J. V. 1970, AJ, 75, 978

Filatov, G. S. 1960, Astron. Tsirk., 215, 20

Geyer, E., Kippenhahn, R., & Strohmeier, W. 1955, Kleine Veröff. Bamberg 11

Hintz, E. G., Hintz, M. L., & Joner, M. D. 1997, PASP, 109, 1073

Hübscher, J., Lichtenknecker, D., & Meyer, J. 1986, BAV Mitt., 43

Hübscher, J., Agerer, F., & Wunder, E. 1992, BAV Mitt., 60

Hübscher, J. 2005, IBVS, 5643

Hübscher, J., Paschke, A., & Walter, F. 2005, IBVS, 5657

Hübscher, J., Paschke, A., & Walter, F. 2006, IBVS, 5731

Hübscher, J. & Walter, F. 2007, IBVS, 5761

Klingenberg, G., Dvorak, S. W., & Robertson, C. W. 2006, IBVS, 5701

Pócs, M. D. & Szeidl, B. 2001, A&A, 368, 880

Rodríguez, E., Rolland, A., López de Coca, P., García-Lobo, E., & Sedano, J. L. 1992, A&AS, 93, 189

SBig Online Product Catalog 2007, (http://www.sbig.com/sbwhtmls/online.htm)

Szeidl, B. 1974, IBVS, 903

Tenagra Observatories, Ltd. 2007, (http://www.tenagraobservatories.com)

Tsesevich, V. P. 1956, Astron. Tsirk., 170

Tsesevich, V. P. 1973, Astron. Tsirk., 775, 2

Zhou, Z.-Y. 2001, A&A, 374, 235